Journal of *Marine Science and Engineering*

MDPI

Article

New Insights into the Seamount Structure of the Northern Part of the Ninetyeast Ridge (Indian Ocean) through the Integrated Analysis of Geophysical Data

Vsevolod Yutsis [1,*], Oleg Levchenko [2], Alexander Ivanenko [2], Ilya Veklich [2], Nataliya Turko [3] and Yulia Marinova [2]

[1] División de Geociencias Aplicadas, Instituto Potosino de Investigación Científica y Tecnológica (IPICYT), San Luis Potosí 78216, SLP, Mexico
[2] Shirshov Institute of Oceanology, Russian Academy of Sciences, Moscow 119991, Russia
[3] Geological Institute, Russian Academy of Sciences, Moscow 119017, Russia
* Correspondence: vsevolod.yutsis@ipicyt.edu.mx; Tel.: +52-444-8342000

Abstract: The linear Ninetyeast Ridge (NER) is the longest oceanic intraplate volcanic edifice and main feature in the Eastern Indian Ocean. Many seamounts are located on the ridge, whose origin and age remain unclear due to the lack of samples of the bedrock of which they are composed. Carbonate sedimentary caps on these seamounts prevent their direct geological sampling by dredging, therefore indirect geophysical methods are an alternative. Such integrated geophysical studies (the main methods are multibeam bathymetry and magnetic surveys) were carried out in cruise #42 of the *R/V Akademik Boris Petrov* in 2017 on a large seamount at the base of the NER's western slope near 0.5° S. The collected data also includes seismic reflection data that reveal morphology, fault tectonics, depth structure, and an assumed origin of this volcanic feature. The Ninetyeast Ridge was formed by the Kerguelen plume magmatism at 50° S in the giant N-S fault. The seamount studied in cruise #42 of the *R/V Akademik Boris Petrov* was formed mainly to the north as a result of two-stage magmatism in a transverse strike-slip fault. The first stage (47 Ma) formed the main western part of the seamount at 20° S. The second stage (23 Ma) formed its eastern part at 8° S. The time intervals between the formation of the main massif of the Ninetyeast Ridge and the stages of subsequent magmatism that formed the western and eastern parts of the seamount are approximately 31 and 55 Ma, respectively.

Keywords: seamount; Ninetyeast Ridge; bathymetry; fault; high-resolution seismic data; reflector; magnetic field; anomaly

Citation: Yutsis, V.; Levchenko, O.; Ivanenko, A.; Veklich, I.; Turko, N.; Marinova, Y. New Insights into the Seamount Structure of the Northern Part of the Ninetyeast Ridge (Indian Ocean) through the Integrated Analysis of Geophysical Data. *J. Mar. Sci. Eng.* **2023**, *11*, 924. https://doi.org/10.3390/jmse11050924

Academic Editors: George Kontakiotis, Assimina Antonarakou and Dmitry A. Ruban

Received: 8 April 2023
Revised: 24 April 2023
Accepted: 24 April 2023
Published: 26 April 2023

1. Introduction

Bathymetric surveys in the world's oceans revealed a large number of seamounts, the vast majority of which were formed at the boundaries of the lithospheric plate, where more than 95% of volcanic activity is concentrated. However, some seamounts were formed away from these boundaries. The explanation of intraplate volcanism required mechanisms and structures other than those that define the tectonics of the lithospheric plates (spreading, subduction, and transform faults). It was suggested that intraplate seamounts are the surface trace of the "hot" mantle plume and can therefore be considered as windows into the Earth's interior, helping to explain various deep processes in the lithosphere [1]. The most important information on the composition and age of rocks composing oceanic structures and, globally, on the chemical and physical properties of the oceanic lithosphere is obtained by analyzing samples raised by dredging and drilling. However, for intraplate seamounts in the world's oceans, such data are very limited; therefore, various geophysical methods are widely used to study them. In the Indian Ocean, there are many seamounts of different ages, the formation of which cannot be explained by a single mechanism [2–7]. The central structure of the Eastern Indian Ocean is the Ninetyeast Ridge (NER), formed according to the "hot spot trace" hypothesis as a result of the Indian Plate drift over the

Kerguelen mantle plume [8–13]. This is evidenced by the results of seven DSDP and ODP deep-water drilling sites due to a regular increase in the age of the basalts along the ridge from south to north from approximately 40 to 80 million years [14,15]. In the existing evolutionary models regarding the nature of the NER, there is generally some disagreement, with the exception of its ancient northern segment, the formation of which is unanimously attributed to intraplate volcanism in the Indian Plate away from the spreading ridge [8,9,13,16,17].

On the main massive body of the ridge, many seamounts were observed along its entire extent, including to the north of the equator [18]. Multibeam echosounder surveys revealed their detailed morphology in different segments of the NER [19–21]. Kopf et al. (2001) proposed that two seamounts in the southern segment of the NER near 17° S are presumably 6 Ma younger than the adjacent parts of the ridge [19]. These conclusions were obtained by correlating seismic profiles through these seamounts with the nearest Site 757 ODP. Attempts to dredge some seamounts in the northern segment on the NER' top in cruise KNOX06RR of the R/V *Roger Revelle* in 2007 were unsuccessful due to sedimentary caps [20,21]. Only from one volcano in the lower part of the western slope of the NER at 10° S in the #55 cruise of the R/V *Vityaz* in 1976 were basalts ~8 million years old dredged [22]. Thus, a young, late Miocene volcanism potentially existed 160 miles north of DSDP Site 214, where the absolute age of the basalts was determined to be between 52.9 and 59.0 Ma, late Paleocene–early Eocene [14,15], which, according to the above authors, cannot be explained within the Kerguelen hotspot model of NER formation or generally from the plume theory.

The sparse grid of vessel magnetic survey profiles determines the weak study of the anomalous magnetic field of the Ninetyeast Ridge, whose structure remains debatable to date. In contrast to the regular series of linear magnetic anomalies in the basins adjacent to the Ninetyeast Ridge [8,9], such single anomalies are rarely identified on the NER rather conventionally due to the limited amount and poor quality of the available magnetic data.

Ideas about the structure and nature of the NER are largely based on the results obtained in regular cruises of the Shirshov Institute of Oceanology (IO RAS) in the 70–80 years of the last century [13,23,24]. In winter 2017, after a long break, cruise #42 of the R/V *Akademik Boris Petrov* resumed geological and geophysical work in the Indian Ocean [25]. One of the tasks of the cruise was to investigate seamounts on the Ninetyeast Ridge. One of them was investigated at the polygon in the area of 0.5° N and 88.8° E (Figure 1). This seamount was selected from the ship's route on the General Bathymetric Chart of the Oceans (GEBCO) Gridded Bathymetry Data [26]. The polygon is located in the northern segment of the NER, which morphologically is a series of echeloned massifs, presumably tectonic blocks, into which it is broken by SW-NW strike-slip faults (Figure 1a) [21–23]. The research included a bathymetric survey using a multibeam echosounder, high-resolution seismic profiling with a parametric profiler, and a hydromagnetic survey. The survey on the polygon was carried out at a speed of 9 knots simultaneously by these three devices on seven profiles with a total length of about 120 km (Figure 1b).

The purpose of this article is to summarize the results from the first detailed geophysical survey of the seamount on the NER to assume the time and origin of this seamount. This allows for the generation of new ideas about the morphology of the seamount based on the new detailed bathymetric survey with a multibeam, as well as new ideas about the deep structure and nature of the mountain based on a detailed magnetic survey performed for the first time. Together, these new results allow us to make assumptions about the tectonic evolution of this NER segment. The new high-resolution seismic profiling data evidence the recent tectonic processes in this area. They confirm the high tectonic activity, which is manifested in the high modern seismicity [27–31].

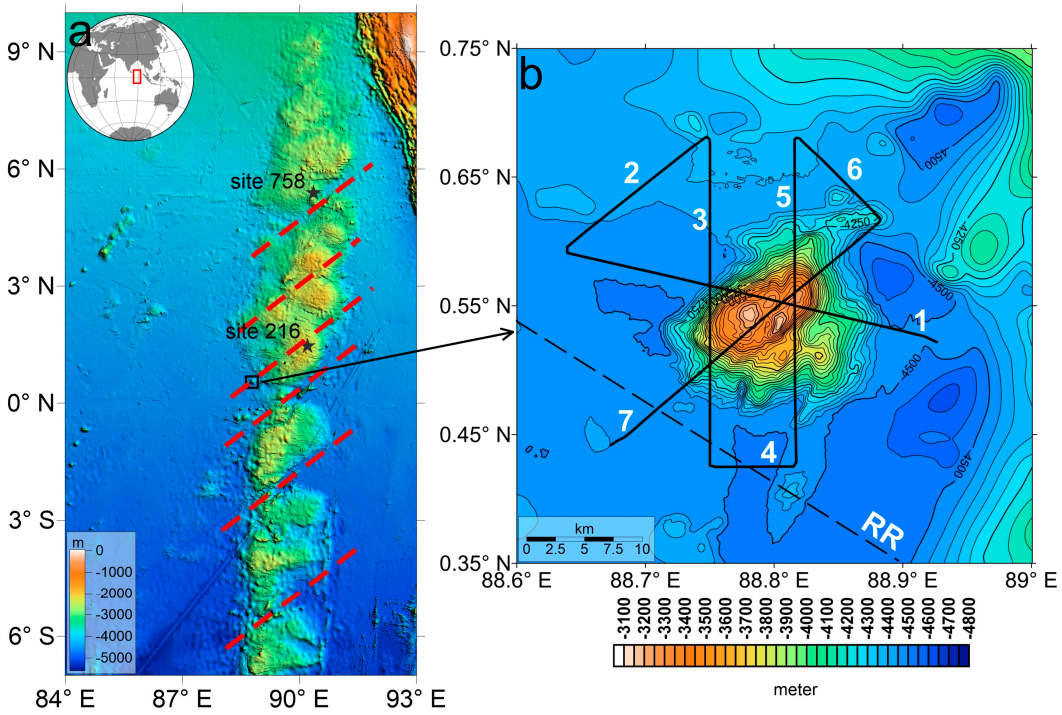

Figure 1. Scheme of the study area: (**a**) echeloned morphology of the northern segment of the Ninetyeast Ridge (position in the inset), GEBCO map base (2019), red dotted line—assumed tectonic faults, and star—deep ocean drilling sites DSDP and ODP; (**b**) bathymetric map with transects of geophysical survey of cruise #42 of R/V *Akademik Boris Petrov* (solid line). Dotted line—profile of the cruise RR1510 R/V *Roger Revelle* (2015).

2. Methods and Results

2.1. Bathymetry

2.1.1. Methods

A bathymetric survey of the seamount with continuous area coverage was performed using the ATLAS HYDROSWEEP DS-2 deep-water multibeam echosounder (ATLAS HYDROGRAPHIC, Bremen, Germany), operating at a frequency of 15.5 kHz. A depth measurement with an accuracy of 0.5% of its value was carried out by 240 beams in wide sector (up to 120°), with the acquisition bandwidth reaching 370% of the depth.

The Hydromap software version 4.2 system data acquisition, processing, and visualization software allowed the survey process to be controlled. During post-processing with the MB-System package [32], the raw multibeam echosounder data were processed (filtered, smoothed, and corrected) and exported from the internal format into ASCII format to calculate a digital elevation model (DEM).

Subsequently, the data for the DEM calculation were supplemented from the GEODAS database [33] with data from the expedition RR1510 of the R/V *Roger Revelle* (2015) that passed through this area [27]. The DEM was used for the construction of the bathymetric map, as well as the calculation of morphometric characteristics, allocation of geomorphological units, etc., in the SAGA GIS program [34]. For the analysis of the relief given below, the data from the seismic profiling by the ATLAS PARASOUND DS2 parametric profiler were also used.

2.1.2. Results

The seamount is located in the lower part of the western slope of the NER at a depth of >4500 m. Its relative height is ~1400 m and the minimum mark is 3093 m (Figures 1 and 2). The base of the seamount on the isobath of 4500 m has an almost rectangular shape of approximately 17 × 15 km. Its longer sides have a SW-NE strike (azimuth ~53°), and

the shorter ones have a SE-NW strike (azimuth ~307°). The top elevated surface of the seamount has a depth of <3300 m and dimensions of 7 × 4 km with an oval-shaped SW-NE strike (azimuth ~53°). On the relatively elevated summit surface, two SSW-NNE ridges extend (azimuth ~25°) 150–200 high. The same SSW-NNE strike-slip faults are also observed deeper in the form of spurs in the lower parts of the slopes. It should be noted that SW-NE and SE-NW strike-slip faults in the northern segment of the NER were previously identified on the detailed survey polygons of the R/V *Marine Geophysicist* and *Pegasus* (1982, 1983) and *Roger Revelle* (2007) [13,20,21]. Both trends are clearly evident in the northern segment of the NER on the General Bathymetric Chart of the Oceans (GEBCO) map [26].

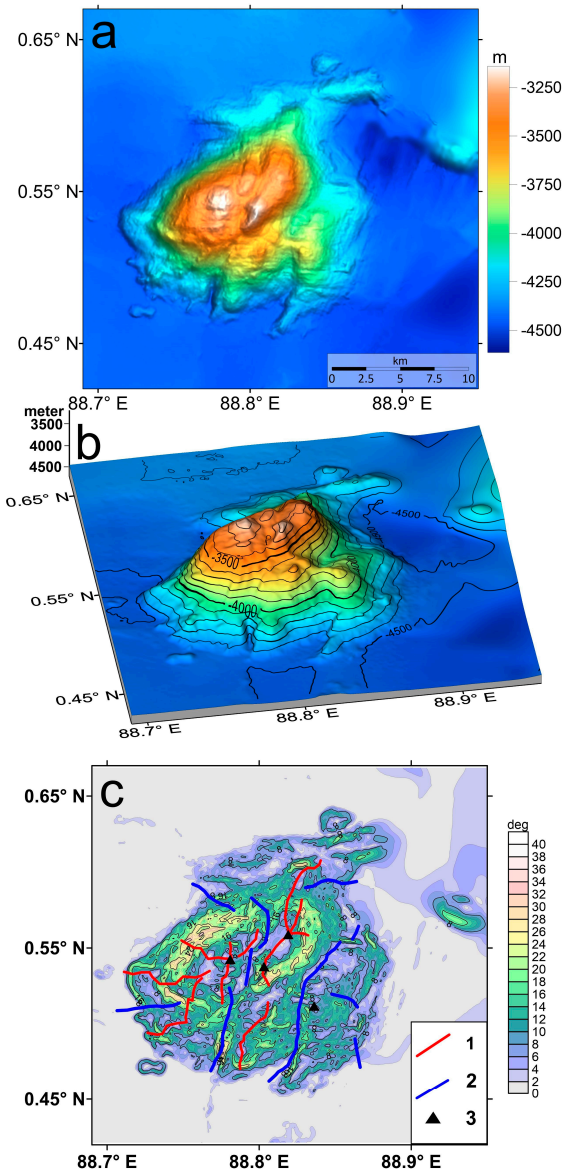

Figure 2. Relief of the bottom of the studied area: (**a**) shaded relief; (**b**) 3D image; and (**c**) map of the slope's dip angles and orographic scheme, 1—axes of rises, 2—axes of depressions, and 3—individual peaks.

The seamount slopes differ significantly in their morphology. The western slope is weakly dissected and steep, with slope angles ranging from 20 to 30–34° (Figure 2c). The southwestern slope is somewhat flatter, with angles of 10–20°, and is dissected by spurs and depressions, as is the northwestern slope. At the foot of the latter, there is a broad protuberance of WSW-ENE trending, formed by separate short ridges. The southeastern

slope of the seamount is characterized by a rather complex relief. In its upper part, the slope angles are 18–25°, and at a depth of 3500–3550 m, a stage of about 1.5 × 2 km is marked, with a conic hill in its center. At a depth of 3800–3900 m, a broad trough separates a step of about 6 km long, in the southern part of which there is also a conic hill more than 150 m high. The slope angles in the lower part of the slope do not exceed 10°, and only in some places on the step ledges does it reach up to 20°.

The morpho-structural analysis of the bathymetric data is obtained, and the bathymetric map of the seamount constructed based on them (Figures 1 and 2) allows us to trace several clear morphological trends, apparently of a tectonic nature. The rectangular shapes of the seamount suggest that the formation of its modern morphology was also influenced by tectonic factors, namely the existing fault zones. The most well-defined are the trends of the SW-NE strike, which are evident in the topography of the seamount and the adjacent section of the NER. These are consistent with the strike-slip structures (Figure 1a) that define the specific echeloned morphology of the northern segment of the ridge [13,23]. The nature and timing of the formation of these SW-NE strike-slip faults in the NER, which possibly continue into the adjacent troughs, are still debatable and are not discussed in this paper. Another distinct morphological trend is the orthogonal SE-NW strike-slip faults, which can be traced in the relief of the basement of the seamount and deeper parts of the polygon. Slightly different trends of SSW-NNE strike are observed in the topography of the upper part of the seamount, with which the ridges on its vault are associated. The troughs separating them are traced into the slope limits and divide the seamount into two massifs (Figure 2). Similar troughs also separate the lower part of the southeastern foothill of the seamount with dissected relief. The features of the seamount's relief are well illustrated by the seismic profiles crossing it (Figure 3).

2.2. Seismic Profiling

2.2.1. Methods

The high-resolution seismic reflection survey in cruise #42 of R/V *Akademik Boris Petrov* was carried out with the parametric sub-bottom profiler ATLAS PARASOUND DS-2. The ATLAS PARASOUND sub-bottom profiler acts as a low-frequency sediment echosounder and as a high-frequency narrow-beam sounder to determine the water depth. The sub-bottom profiler is based on the parametric effect, which is produced by additional frequencies through nonlinear acoustic interaction of finite amplitude waves. If two sound waves of similar frequencies (18 kHz and e.g., 22 kHz) are emitted simultaneously, a signal of the difference frequency (e.g., secondary low frequency of 4 kHz) is generated for sufficiently high primary amplitudes. This new component travels within the emission cone of the original high frequency waves, which are limited to an angle of only 4.5° for the equipment used. The penetration was up to ~80 m into the seafloor.

PARASOUND seismic data were recorded during all cruises in parallel with the bathymetric survey. The study area included seven profiles, four of which crossed the mountain. Unfortunately, due to technical and weather problems, the quality of the materials is not high. The data obtained, which were recorded onboard with an SEG-Y format, were processed using the RadExPro 2019.1 software. The workflow of the processing consisted of the following steps: frequency filtering, muting, static correction, equalization of the amplitudes, deconvolution, etc. IHS Kingdom Suite software version 8.8 was used for interpretation, visualization and construction of 3D images, as well as for time/depth conversion by section. The geological interpretation of sub-bottom profiles was carried out based on the criteria of seismic stratigraphy in order to identify the main seismic sequences [35–37]. We integrated available core data from the following sources for interpretation of sedimentology: core data from Ocean Drilling Program (ODP) Leg 121 Site 758 (05°23.04′ N, 90°21.66′ E) and International Ocean Discovery Program (IODP) Leg 353 Site 1443 (5°23.01′ N, 90°21.71′ E) [15,38]. These sites were drilled ~550 km north of the study area. In the nearest Site 216 Deep Sea Drilling Program (DSDP) (01°27.73′ N, 90°12.48′ E), no samples were taken from the upper part of the section [14]. The drill sites

have similar depositional environments; therefore, we assumed that the sedimentology and physical properties did not vary significantly.

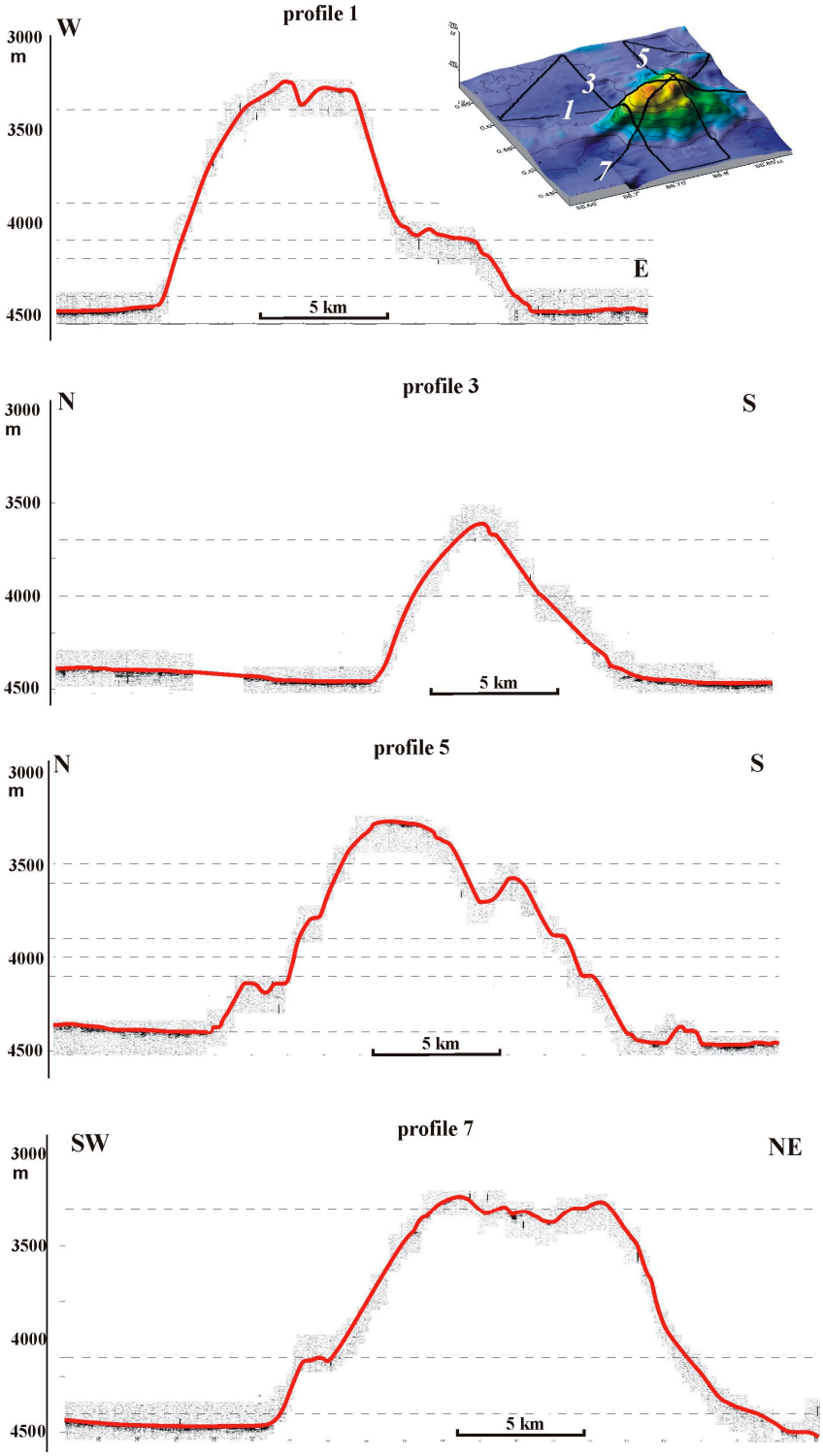

Figure 3. Seismic profiles of the ATLAS PARASOUND DS2 parametric sub-bottom profiler on a very compressed scale through the seamount. The seafloor is highlighted in red. The location of the profiles is shown in the inset above and in Figure 1b. More detailed portions of some seismic profiles are shown in Figure 5a (Profile 5) and Figure 6b (Profile 3).

2.2.2. Results

The visible thickness of the sedimentary cover according to seismic data is not constant. It varies from a few meters to 80–100 m in the northwestern part of the study area. The four seismic profiles crossing the seamount show no reflection boundaries in the sedimentary cover on the seamount (Figure 3). The sediment structure with internal reflectors below the bottom surface is really not visible due to the very compressed and very small scales of the PARASOUND records. Furthermore, volcanic rocks composing the seamount are exposed directly in the bottom surface, and acoustical seismic signals do not penetrate normally below the seafloor here. Unconsolidated loose sediments with a thickness of several meters are found here only in small depressions on the seamount. This pattern is typical for seismic reflection profiles through seamounts. Therefore, the records of the sub-bottom profiler PARASOUND with a high frequency of 4 kHz look similar to a recording of a single-beam echosounder.

The visible thickness of the sedimentary cover areas off the seamount slopes reaches 80–100 m (Figures 4–6). An analysis of the wave pattern of the seismic records in the northwestern part of the study area made it possible to identify three seismo-stratigraphic units, whose boundaries correspond to horizons named A, B, and C (Figure 4). Prominent seismic reflectors/horizons were traced visually based on their characteristic reflection pattern, amplitude, and continuity.

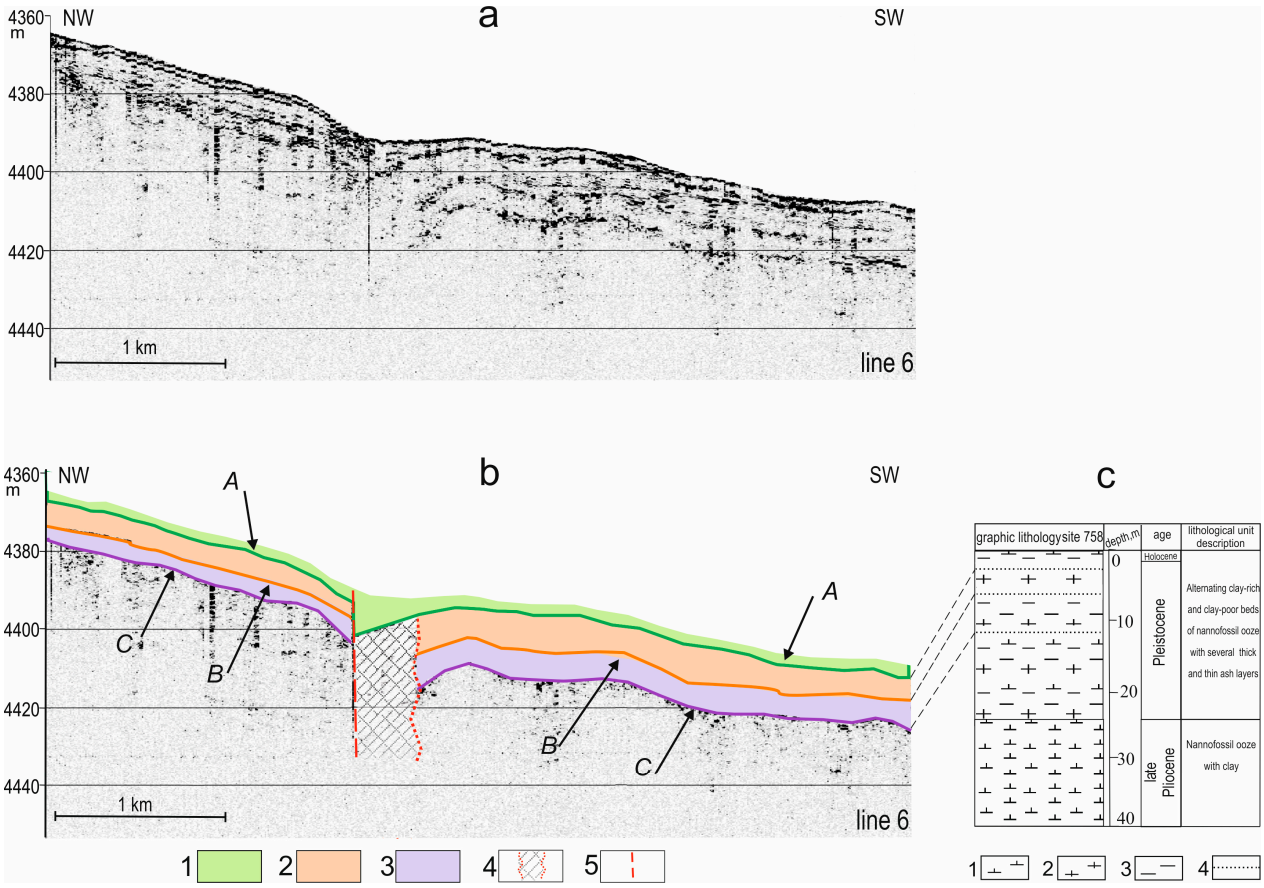

Figure 4. Seismic line 6 north to the seamount: (**a**) original uninterpreted and (**b**) interpreted. Reflectors A, B, and C are shown by green, orange, and violet lines. 1—seismo-stratigraphic unit 1; 2—seismo-stratigraphic unit 2; 3—seismo-stratigraphic unit 3; 4—disturbed zone with a chaotic acoustic structure and no of correlation of reflectors; and 5—fault. It was not possible to identify the seismo-stratigraphic unit below reflector C. The position of line 6 is shown in Figure 1a. (**c**)—lithostratigraphic summary of Site 758 ODP. 1—clayey nannofossil ooze; 2—nannofossil ooze; 3—clay; and 4—volcanic ash.

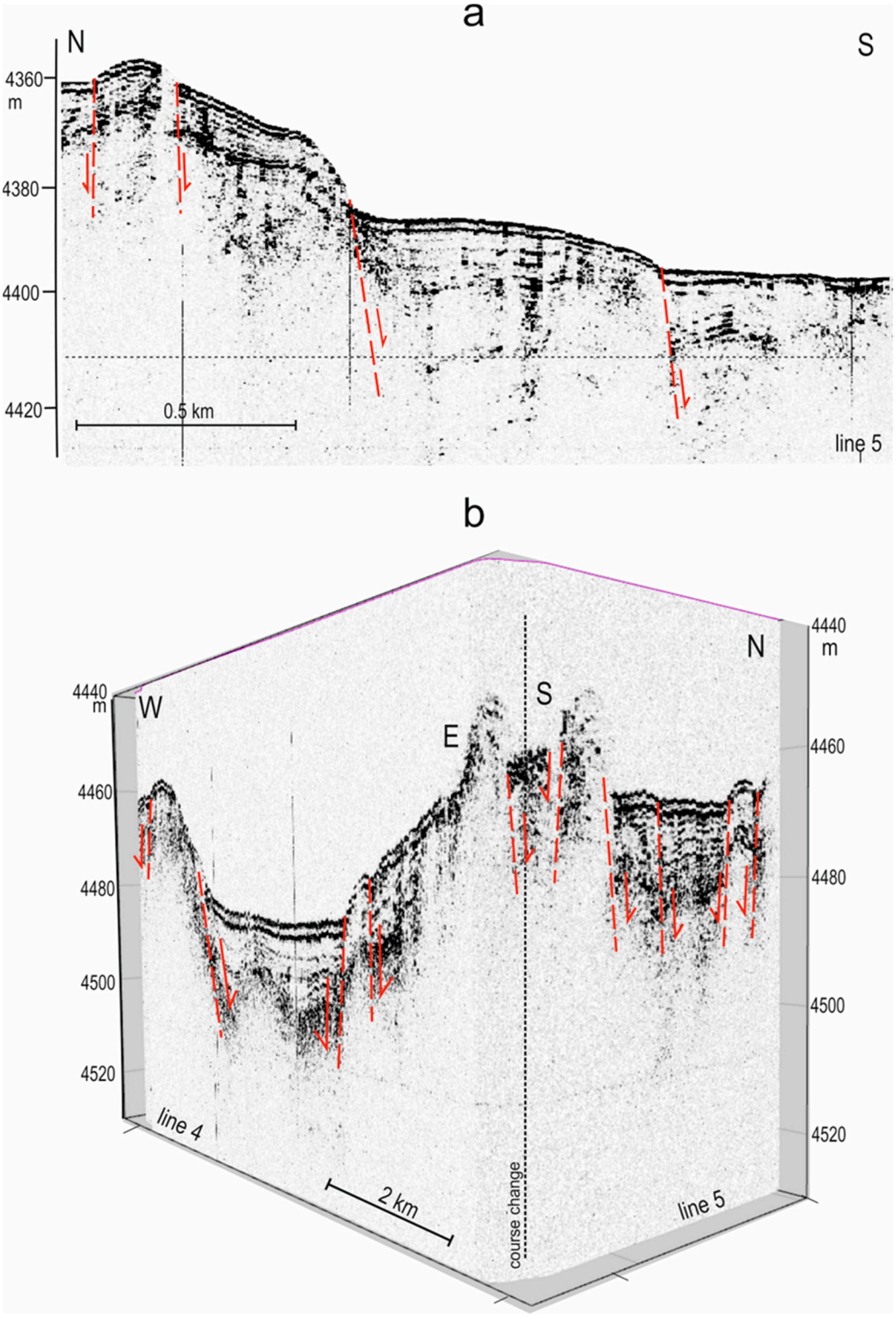

Figure 5. The PARASOUND profiles near the seamount slopes showing fault possible activity. (**a**) Profile 5 north to the seamount. (**b**) Profiles 4 and 5 south to the seamount. Possible faults (red dotted line) in the upper part of the sedimentary section, coming to the bottom surface. The red arrows show the direction of displacement along the fault. The position of the profiles is shown in Figures 1b and 3.

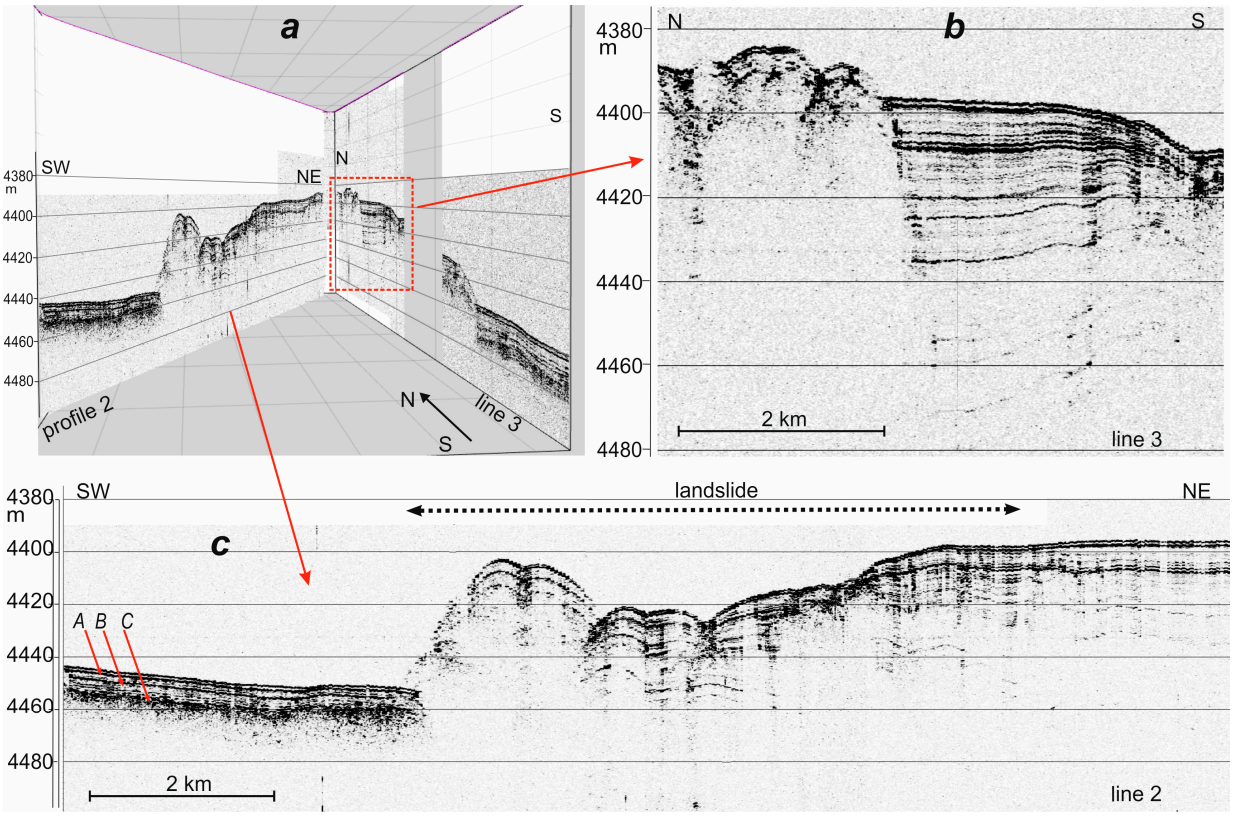

Figure 6. Fragments of seismic profiles 2 and 3 through the landslide bodies in the north of the polygon. (**a**) common view; (**b**,**c**) view in details. The position of the profiles is shown in Figure 1b. Reflectors A, B, and C in (**c**) mark possibly the ash interlayers.

Seismo-stratigraphic unit 1 is located between the bottom and reflector A and has a thickness of about 2–3 m. It is traceable in all seismic sections. reflector A is a continuous, high-amplitude, relatively smooth boundary that almost conformally repeats the bottom topography. Then, seismo-stratigraphic unit 2 follows, the bottom of which is the boundary B. It is characterized by acoustic facies with parallel, high-amplitude discontinuous reflectors. Reflector B stands out at a depth of 7–9 m; it has a lower amplitude and is more discontinuous than reflector A. Seismo-stratigraphic unit 3 has seismic facies with parallel, high-amplitude continuous to discontinuous reflectors. The lower boundary C at a depth of 11−15 m stands out in some places, more often being a series of close intermittent high-amplitude reflections. Below seismo-stratigraphic unit 3, no layering can be traced in our seismic sections.

These reflectors mark the geological boundaries of sediment layers with different physical properties of sediments, primarily density, which is usually due to changes in their lithology. For the lithological and stratigraphic interpretation of seismic profiles, the results from deep ocean drilling sites 758 and 1443 [15,38] were used. We understand that our sections did not cross the drilling sites. Nevertheless, we are trying to give a lithological characteristic to seismo-stratigraphic units. The sites are close to each other and have a similar section. For analysis, we studied the top of section of Site 758. The upper part (0–25 m) of it consists of alternating clay-rich and clay-poor layers of nannofossil ooze with several thick and thin ash layers. Deeper than 25 m of nannofossil ooze with clay was drilled. At a depth of 2 m, the first ash layer of up to 10 cm thickness was identified in the core section. We suppose that the high-amplitude reflector A in the seismic section is correlated with this ash layer (correlation lines are shown by a dotted line between Figure 4b,c), and seismo-stratigraphic unit 1 represents nannofossil ooze.

At a depth of 8 m, an ash layer up to 23 cm thick was identified in the site core. Possibly, reflector B is associated with the appearance of this relatively thick ash horizon in the sedimentary section, and seismo-stratigraphic unit 2 is nannofossil ooze with clay and frequent interbedding of thin layers of ash. In this interval, a change in physical properties is also noted: a decrease in $CaCO_3$ content and a slight increase in density. One of the largest layers of ash for this section is noted at a depth of 11 m and has a thickness of 13 cm. Perhaps this ash layer is the C boundary. The seismo-stratigraphic unit 3 also represents clayey nannofossil ooze. The sediments are more bioturbated and contain less ash layers. Furthermore, this core interval is characterized also by a change in physical properties: a decrease in $CaCO_3$ content and a slight increase in density. Thus, there is a rather high degree of correlation between seismic reflectors and the lithology of the upper part of the sedimentary section. According to core data, we suppose that seismo-stratigraphic units 1, 2, and 3 can be placed in the Holocene–late Pleistocene age.

The northeastern part of the Indian Ocean south of Hindustan is characterized by high tectonic activity manifested by intense crustal fracture deformation and the highest oceanic intraplate seismicity [28–30]. This zone of intense intraplate deformation also captures the northern segment of the Ninetyeast Ridge [15]. Here, strong aftershock events of two mega-earthquakes of a magnitude of around 9 continued in the adjacent Warton Basin [31]. It is believed that the high seismicity of the NER may be related to faults extending down to the bottom surface [20,21]. Our seismic profiles near the seamount show some signs of young, possibly modern neotectonic fault activity in the uppermost part of the sedimentary sequence (up to 50–80 m) (Figure 5). Considering the distortion scale, the faults are relatively gentle normal faults and have a small displacement amplitude. The data obtained do not allow us to trace them in depth.

Further evidence of modern tectonic activity on the seismic profile are the acoustically opaque zones with a chaotic internal sedimentary structure and an uneven bed (Figure 6), which we interpret as landslide sedimentary bodies. The landslide is located in the northwestern part of the study area. The source area was observed as chaotic, discontinuous, low-amplitude reflectors in the reflection seismic data were collected, with some continuous stratigraphy visible. The observed pattern is in good agreement with the classical landslide structures on the slope of marine tensional depressions and compressional elevations [39]. Reflectors A, B, and C were determined in the southwest part of the profile and have sharp contact with the frontal deformation landslide zone. At first sight, the vertical boundary, at which the reflectors abruptly cut off, may appear as a steep fault (Figure 6b); however, this is due to a strong distortion of the recording scale (horizontal scale/vertical scale = ~30). On the profile transformed to a more realistic view, which is not given in the paper, this boundary is quite flat and characteristic of the landslide edge.

2.3. Magnetic Survey

2.3.1. Data and Methods

The hydromagnetic survey in cruise #42 of R/V *Akademik Boris Petrov* was carried out with the MPMG-4 magnetometer (IO RAS production). A map of the anomalous magnetic field (AMF) was synthesized based on the data of this cruise collected at the studied area and the results of two surveys from the National Centers for Environmental Information, NCEI database [40] (Figure 7a). The RMS error in the survey is estimated from the 20 profile intersection points to be 6.3 nT, which is just over 1% of the AMF amplitude over the seamount. This is a good result for open oceanic areas. To estimate the depth to the center of magnetic masses, we apply the generally recognized method [41], which also uses a radially averaged, frequency-normalized spectrum of magnetic anomalies.

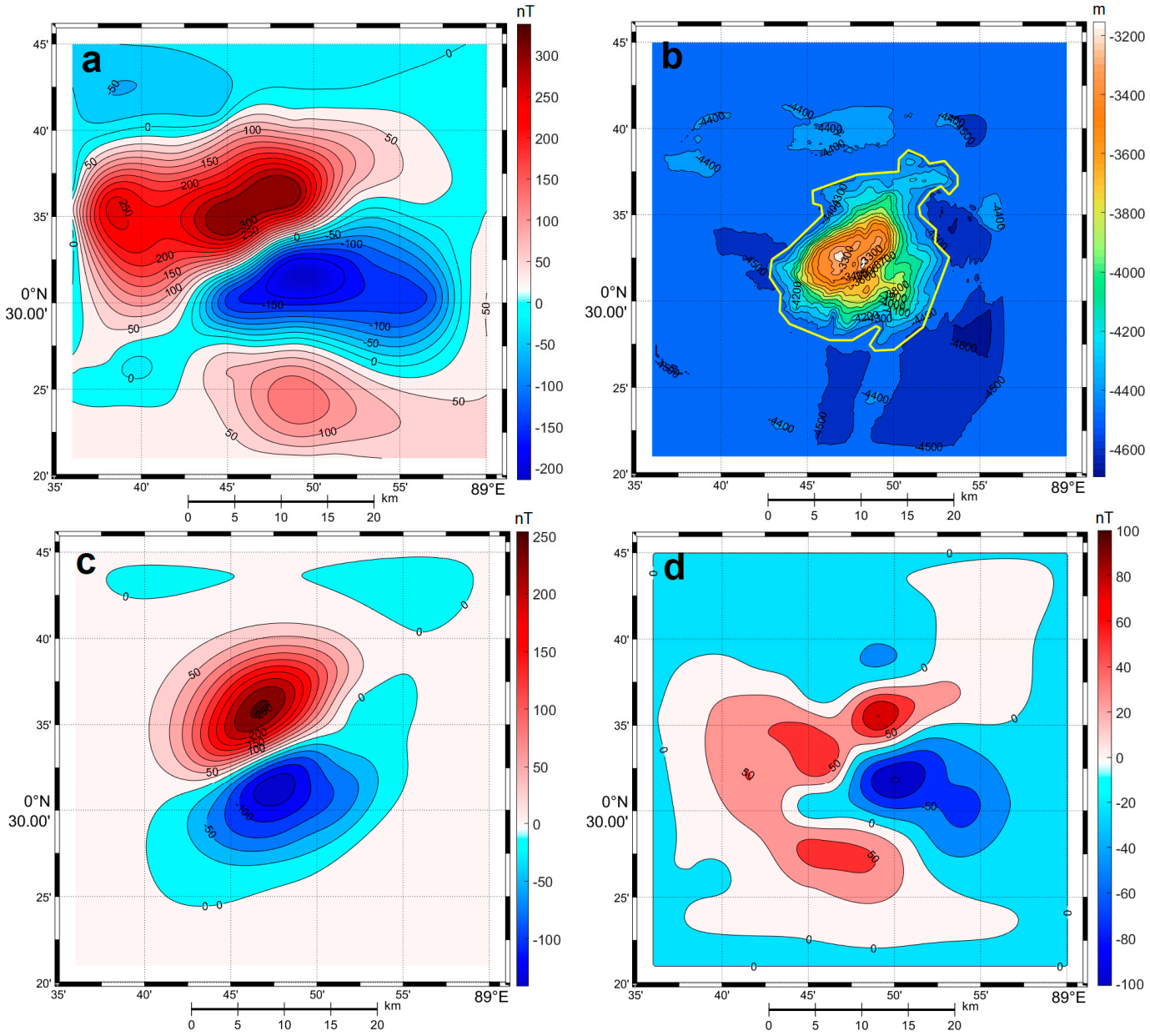

Figure 7. Anomalous magnetic field (AMF) above the seamount and testing of the hypothesis of homogeneous magnetization of this structure: (**a**) measured field synthesized from geomagnetic surveys, in nT; (**b**) seamount topography and contour (yellow bold line) limiting the position of the homogeneous source in the horizontal plane, in m; (**c**) model AMF with a homogeneously magnetized seamount, in nT; and (**d**) residual field (measured−model), in nT.

2.3.2. Results

An intense (>540 nT) alternating magnetic anomaly, extending from SW to NE, is observed above the studied seamount (Figure 7a). The zone of the largest AMF gradients is confined to the seamount top. This gradient zone of NE extension (azimuth 60–65°) separates rather smooth positive and negative parts of the anomaly. Its positive branch is located above the northern slope of the seamount and continues into the adjacent deep-water basin. It has two local maxima of approximately the same amplitude +305 nT and +280 nT to the north of the oval top. This indicates a possible inhomogeneity of the magnetization of the seamount. The negative branch of the anomaly with one minimum ~−240 nT is located above the southern slope of the seamount as well as in the adjacent

deep-water basin. It is important to note that the main part of the magnetic anomaly (>150 nT module, i.e., about 0.5 of the maximum amplitude) covers an area much larger than the seamount foot along the 4500 m isobath. This may indicate that the magnetic field in this section of the NER reflects not only the actual relief of the ocean floor, but also deeper sources. In addition, the area of maximum AMF amplitudes is to the north of the seamount, which is a characteristic of normally magnetized objects in the Southern Hemisphere.

A three-dimensional interpretation of the magnetic anomalies over the seamount was performed and includes an analysis of the morphology of AMF and its gradients, in order to highlight the structural boundaries and features of the spatial distribution of the anomaly sources [42–45]. The key issue for this object located practically on the equator was to determine the direction of its magnetization, since the correct analysis of the AMF morphology and its gradients requires a reduction in the anomaly to the pole. This problem was solved by successive application of the methods of the area analysis of AMF—the Helbig magnetic moment method [46] and the method of interactive selection of the equivalent source geometry, with a calculation of the average magnetization vector by the least squares method. Both independent methods yielded results that are close in inclination, -41° and -45°, but quite different in declination, -62° and -27°, respectively. This difference is explained by the fact that the magnetic moment method is more sensitive to edge effects and misaligned anomalies [47], which are obviously present in our data (see Figure 7a). The analysis of the morphostructure of the analytical signal suggests that structural lineaments orthogonal to its strike, possibly limiting faults, adjoin the southwestern and northeastern edges of the main magnetic source. The morphostructure of the analytical signal shows evidence of two centers in the deep structure of the object confined to its flanks, which confirms the modeling results.

To estimate the magnitude and direction of the average magnetization of the seamount, we also used the simplest model of a uniformly magnetized seamount; the results of this fitting are shown in Figure 7b–d. These results clearly show that the magnetic structure of our object is significantly more complex. The residual anomalies clearly demonstrate the presence of at least one more intense source of anomalies in the NE part of the structure. Therefore, we complicated the model and divided the volume of the seamount, considering the morphostructural analysis performed, into four parts: two in the apical part, while the other two are confined to the NE and NW slopes. However, in the process of solving the inverse problem for four uniformly magnetized bodies, it turned out that the calculated magnetization directions of the central and peripheral bodies practically coincide in pairs. Therefore, we left the segmentation into the central and peripheral parts of the seamount as the main one. Further interpretation was performed under the assumption that the magnetization direction changes insignificantly within the given blocks (the geological–structural inverse problem, according to [48]).

Before the vector three-dimensional interpretation, we also estimated the depth to the lower edge of the sources of magnetic anomalies. During the selection of the simplest models, the depth of the base of the model blocks was successively changed with a step of 0.5 km in the range from 4.5 to 8 km. The best selection corresponded to the depth of the seamount base at 7 km from the ocean surface (2.5 km deeper than the bottom of the adjacent basin). The estimate obtained by the widely used spectral method [49,50] has the same value: 7.08 km. Therefore, in further constructions, the lower edge of the models was fixed at a depth of 7.1 km from the ocean level (2.6 km below the bottom in the seamount area). It should be noted that the field morphology analysis and model selection were carried out with simultaneous use of field data and their gradients, which significantly increased the stability of the interpretation.

The determination of the average depth to the upper edge and center of magnetic masses showed that the main depth interval, in which the sources of the anomaly are located, is 3.5–7.1 km from sea level. This indicates the presence of the deeper roots of the investigated seamount and indicates its volcanic nature.

The results of solving the inverse problem, i.e., finding the vector inhomogeneous magnetization in the volume of the mountain, are presented in Figure 8. We obtained an almost complete coincidence between the measured (Figure 8a) and model (Figure 8c) fields (correlation coefficient > 0.99). To verify the model, we also used the solution of the direct problem with the found magnetization values, but under the condition of the verticality of the magnetization vector and the direction of the external field - an analog of reduction to the pole (Figure 8d), which is usually performed only by the AMF maps [45]. The direct correlation of the obtained anomaly with the relief (Figure 8b) is obvious, as well as the confinement of the high magnetization values (Figure 8f) to the main volcanic structures of the seamount—its central two-top block—located inside the white dotted line in Figure 8b. The seamount is characterized by magnetization values up to 5.7 A/m with an average value of 3.2 A/m, which are normal for this type of volcanic structure.

The magnetization vector directions obtained by solving the inverse problem were recalculated into the paleolatitudes and age of the formation according to global modern paleo-reconstructions. For each elementary volume in the seamount body, we can determine the direction of this vector, and hence, the paleolatitude of its formation by the found value of the magnetization vector, assuming that the magnetization, such as that of most igneous rocks in the ocean, has a predominantly remanent component. Next, we used the relationship between the paleolatitudes and age for any point on the Earth [51], based on the modern paleotectonic reconstructions, to recalculate the paleolatitudes we found into the ages. The magnetization directions calculated for the volume of the seamount form two clusters with average values of -36° and -16°, respectively, for the central and peripheral blocks. These inclination values correspond to the paleolatitudes of 20° S and 8° S. The results of determining the age of the seamount sections are presented in Figure 8e. The proximity of the boundaries of the same-age areas to the dividing of the seamount set at the first stage of the interpretation is noteworthy; apparently, this approach was successful, which was confirmed by checking the recalculation of the magnetization in the poleward anomalies. In general, the patterns of the age distribution of the seamount structures are as follows: the central part of the structure, including smoother and steeper western and northern flanks, is about 47 Ma. Less regular, gentler eastern and southern flanks with numerous small uplifts and depressions are about 23 Ma. Such a significant difference indicates at least a two-stage volcanic development within the studied seamount.

In Figure 9, which shows the distribution of the magnetization modulus within and under the volume of seamount, we noticed a thick central body extending from SW to NE (the isosurface is given for magnetization values I = 3 A/m), which is located directly below the oval top of the seamount. The ratio of the horizontal axes of this body is close to 2.5, and the strike azimuth completely coincides with the morphological trends of the seamount.

According to the complex of the studied seamount's geological and geophysical parameters and the results of their interpretation, it becomes obvious that the most adequate explanation of the observed phenomena is the process of volcanism development along the NE strike-slip fault. This volcanism, which originated on the NE strike-slip fault and began 47 Ma ago, led to the growth of almost 3.5 km (considering the thickness of the modern sedimentary cover—up to 2 km [52]) of a conical structure, which we observe as the central part of the seamount. As the paleo-volcan grew, the center of the effusion shifted along the fault to the NE, and then volcanism ceased after a short time. The short duration of this phase of volcanism follows from the fact that the studied seamount has a direct polarity magnetization, and in the middle Eocene, chrons of direct magnetic polarity are less prolonged than those of reversed polarity. The most likely straight magnetic polarity chron, during which our object was formed, is 21n, which began 48.88 and ended 47.76 Ma ago [53]. Intense volcanism resulted in the formation of a regularly shaped seamount extending in the NE direction and up to 3.5 km high.

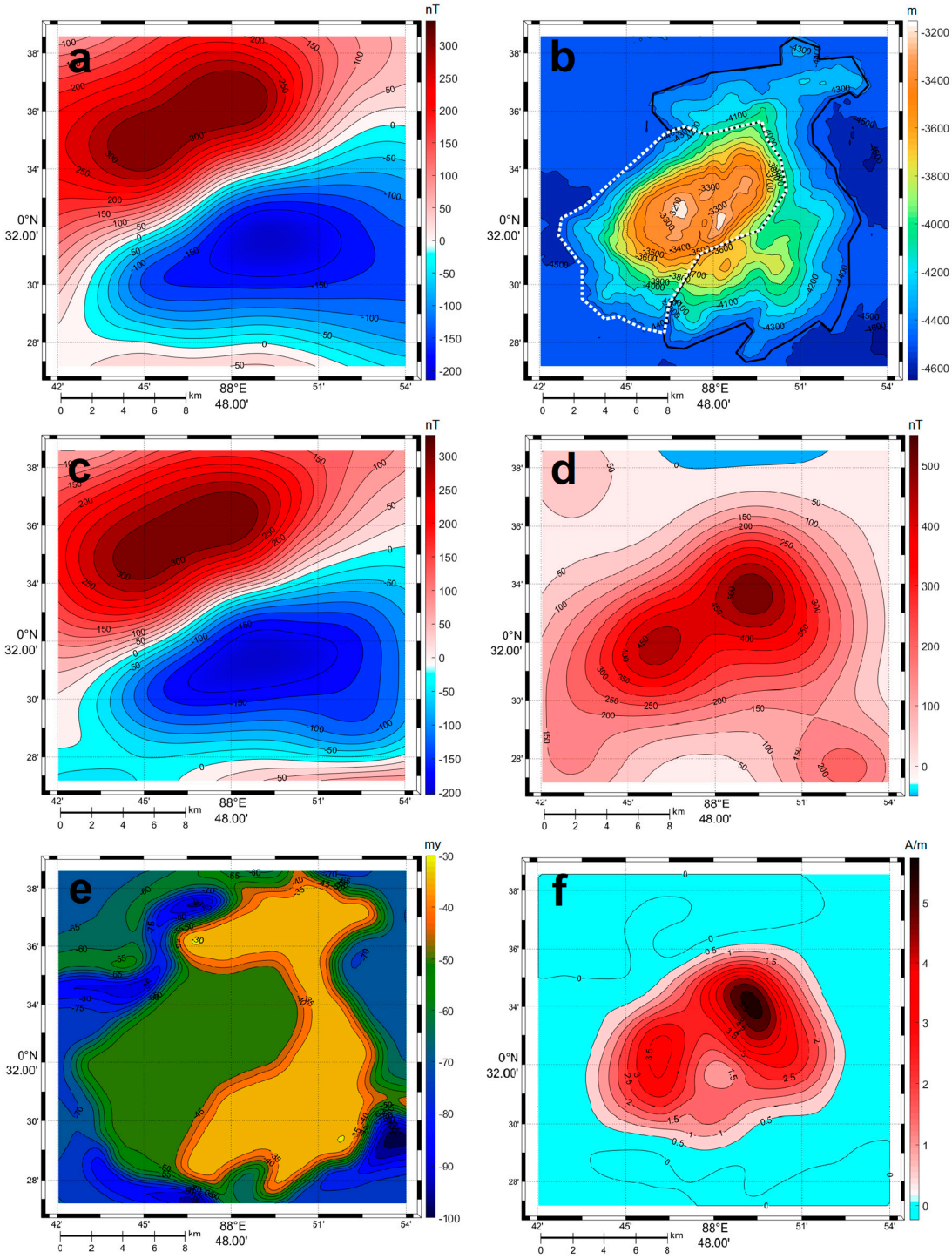

Figure 8. Results of solving the inverse problem — finding the inhomogeneous magnetization in the volume of the seamount: (**a**) the initial AMF directly over the seamount, nT; (**b**) the division of the relief into two main blocks (white dashed and black bold lines), for which the average magnetization directions were previously determined and fixed as constraints; (**c**) the model field from the picked magnetization distribution, nT; (**d**) solution of the direct problem with the selected magnetization distribution, provided that its direction and the direction of the external field are vertical (reduction to the pole), nT; (**e**) age of the seamount fragments, determined by recalculating the found dip angles into the paleolatitude and age using paleo reconstructions, Ma; and (**f**) lateral distribution of magnetization, A/m.

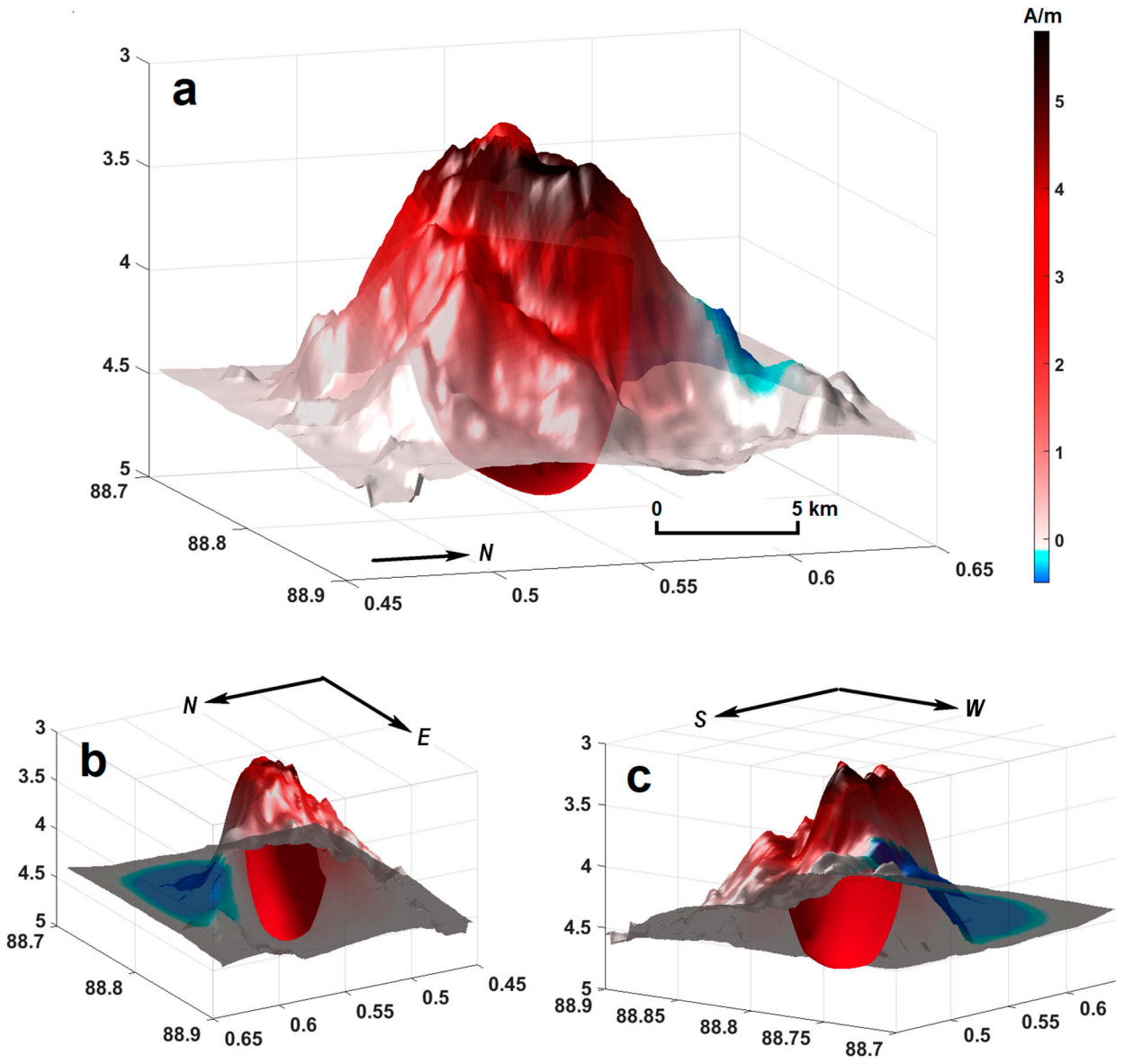

Figure 9. Solution of the inverse problem - finding the inhomogeneous magnetization in the volume of the seamount: (**a**) magnetization, A/m. The isosurface corresponds to 3 A/m. (**b**) The isosurface, bottom view from the NE. (**c**) The isosurface, bottom view from the SW.

Volcanism at the study area resumed about 23 million years ago. The center was confined to the NE summit, but for a number of reasons (a topic beyond the scope of this article), the main effusion occurred in the eastern and SE segments of the structure, and precisely on the seamount slopes, not on its summit. As a result, a characteristic morphology of the structure and a peculiar magnetic structure of the anomaly sources were formed.

3. Discussion

Seamounts are widespread in the Eastern Indian Ocean [2–7]. Many seamounts are located on the Ninetyeast Ridge [19–21]. However, their age and origin are still largely undetermined, as no samples of their bedrock were recovered. The prominent seamount at the base of the NER in its ancient northern segment was investigated by an integrated multidisciplinary detailed geophysical survey in cruise #42 of R/V *Akademik Boris Petrov*. The detailed maps of the topography from the collected multibeam data and the anomalous magnetic field of the surveyed area were constructed the first time. As a result of the

bathymetric survey, the morphology of the seamount was significantly clarified. It was found that the bottom relief here has several clear morphological trends of SW-NE, SE-NW, and SSW-NNE strike, which most likely mark the faults. The results obtained are consistent with existing ideas about the tectonics of the northern segment of the NER and add new details to them. Furthermore, the results allow us to make assumptions about the role of the tectonic factor in the formation of the seamount and the possible timing of the volcanism that formed it. The assumption of two stages of fault-related magmatic activity is fundamentally new.

The formation of the main massif of the studied seamount appears to be related to magmatism along the SW-NE strike-slip fault. Two small ridges on the mountain vault are probably associated with the manifestations of magmatic activity along the SSW-NNE strike-slip faults. The strike of the distinguished faults does not coincide with the N-S (transform fracture zones) and E-W (faults in the paleo spreading center) strike of spreading fault structures in the Eastern Indian Ocean [8,9], i.e., they have a different nature and formation time (apparently, more recent). Based on the geomorphological analysis of rare echosounding profiles, some influence of fault tectonics on the formation of the modern bottom topography of the northern segment of the NER [21], located immediately north of the polygon, was previously admitted. The volcanic nature of the ridge itself and its formation as a result of a massive outpouring of basalts in shallow/subaerial conditions is confidently supported by the results of petrological, lithological, and biostratigraphic studies of deep-water drilling cores [14,15,54]. However, this does not exclude a younger subsequent stage of volcanism, which could partly be controlled by fault tectonics.

The flat summit surfaces of the seamounts on the NER vault for the section located immediately north of the polygon are explained by possible erosion activity in subaerial conditions [18]. The elevated summit of the seamount we investigated cannot be related to such a factor. It lies much deeper than it could if submerged after formation from the ocean surface, both according to the theoretical and actual graphs of aseismic ridge submergence, including the NER [54]. Apparently, its morphology with a relatively elevated top is caused by endogenous factors related to the peculiarities of the NER volcanism, and probably, by alignment as a result of pelagic sedimentation and subsequent redistribution of sediments by local exogenous factors.

In the northeastern part of the Indian Ocean, traces of volcanic activity of the Indonesian island arc are widespread in the quaternary sediments. The products of volcanic activity (ash, tephra, and lapilli) in the form of 5–40 cm-thick interlayers were found in many deep-water sites [14,15]. Using tephrochronology, geochemical, and mineralogical analyses, it was established that the ash layers in the upper part of the core section of Site 758 are the result of four stages of the eruption of the Toba volcano on Sumatra Island [55]. Its last eruption (75,000 BP), when volcanic ash covered an area of ~4 million km^2 all the way to the east coast of Africa, was one of the largest in the last 25 million years. An analysis of our seismic data, performed with stratigraphic reference of deep-water drilling data, revealed that the three main reflectors A, B, and C (Figure 4) are possibly associated with the presence of ash interlayers. Their wide distribution within the study area may be associated with the eruptions of the Toba volcano on Sumatra Island.

Furthermore, the seismic data obtained significantly complements the ideas about high neotectonic, up to modern, activity in the northern part of the Ninetyeast Ridge. They confirmed the existence of faults in the uppermost part of the sedimentary cover up to the bottom surface, with which, as suggested by [20,21] high regional intraplate seismicity, they may be associated. Further evidence of modern tectonic activity may be the discovery of a sedimentary body with a chaotic internal structure, which appears to be of a landslide nature.

The small low depression is in the seafloor in the central part of profile 6 (Figure 4). Reflectors A, B, and C bend the immediate in its vicinity and then they abruptly break off, apparently on a fault scarp. Existence of a disturbed zone with a chaotic acoustic structure and no correlation between reflectors B and C is related apparently to tectonic deformation. However, an increased thickness of sediments above reflector A may indicate some activity

of any small gravity flow that created a low channel. There is some alternative to its genesis (paleochannel or fault zone) due to the scarce penetration.

The magnetic survey over the seamount registered an intense magnetic anomaly, which is much larger in area than the base of the seamount. It was established that the main source of this anomaly is a deep linear geological object of SW-NE strike, located under the basalt layer of the oceanic crust. Apparently, the deep roots of the seamount are associated with the manifestation of magmatic activity in the zone of one of the faults of such a strike, previously identified in the northern segment of the NER by morphological features [20,21]. It is necessary to explain why the two identified positive local magnetic anomalies in the polygon are slightly offset relative to the ridges in the bottom topography at the top of the seamount. Apparently, the ascending magma flow had a lateral horizontal deflection from the deep source, which creates these anomalies, and magma migrated upward along the already existing weakened fracture zones in the ridge body, which was potentially somewhat distanced from it. A similar setting was previously observed in the formation of relatively young volcanoes to the south on the NER vault during horizontal magma flow [19].

The results of the interactive selection of the equivalent source of magnetic anomalies clarified our preliminary assumptions, which were made on the basis of the geomorphological analysis, about the two-stage formation of the seamount. The obtained values suggest different paleolatitudes of the formation of the isolated segments of the seamount in the two-stage cycle of its formation. According to our calculations of the paleolatitude and age according to the magnetization vector of the seamount, its southwestern part was formed at the first stage approximately 47 million years ago, and later the northeastern part approximately 23 million years ago. At the same time, apparently, two small volcanic structures on its top were also formed. Initially, in our opinion, after the formation of the main volcanic massif of the ridge here in the next phase of secondary outpourings, the more ancient western part of the seamount was formed. Then, during the subsequent phase of magmatic activity, it expanded in the eastern direction. At the same time, the source of magmas, judging by the close values of the estimates of the residual magnetization value, remained the same. As a result, a linear (aspect ratio ~3:1) single object of the northeastern strike apparently formed by magmatism in the zone of one of the faults of the same strike, and was previously identified by different researchers in the northern segment of the NER from the analysis of its morphology [13,20,21].

The explored seamount at 0.5°N lies on the boundary of two segments of the NER that differ sharply in their depth structure. The segment to the south of 0.5° N is characterized by a low effective elastic lithospheric thickness (Te) 0–5 km, whereas the segment to the north is much higher in thickness 10–20 km [16,56]. The formation of this boundary is associated with the second phase of spreading in the multistage late Cretaceous–Cenozoic evolution of the Eastern Indian Ocean and the first major reorganization of plate kinematics about 53 Ma ago during the first soft continental collision of the Indian continent with the island arc of the South Asian subduction zone [8]. The interaction of the Kerguelen mantle plume with the paleospreading ridge potentially created a thermal anomaly that disrupted the oceanic lithosphere and excessive magmatism [12,13]. The timing of the first phase of the formation of the seamount we studied, 47 Ma, closely follows this dramatic event. The third phase of spreading began in the Middle Eocene ~42 Ma, when the second major reorganization of the plates in the Eastern Indian Ocean occurred due to the hard collision of the Indian Plate with the Eurasian Plate - the continental collision of Hindustan with Asia [8], which continues to the present day. The second stage in the formation of the seamount we studied, 23 Ma, seemed to be related to the reorganization of the fault when the stress created by the collision in the northward drifting Indian lithospheric plate reached critical values.

The mechanism of the formation of the studied seamount may be identical to the previously proposed underplating mechanism. It explained the nature of two relatively young volcanoes to the south on the vault of the central segment of the NER near 17° S, which

formed 6 Ma later than the main structural phase of the ridge [19]. The aforementioned authors associated the latter phase of volcanism with the relaxation of tensile stresses in the attenuated NE-SW strike-slip lineaments and magma uplift along the small pool apart structures that formed. These stresses could create a regional tectonic and/or heat source beneath the ridge due to an anomalous hot spot regime. They believed that the weakened NE-SW and NW-SE strike-slanted lineaments, obliquely oriented relative to the main regional meridional tectonic structures, were potentially formed by left-lateral strike-slip faults along a giant 90° E fracture zone [21]. The tectonic faults identified by the polygon survey are in good agreement with these directions. A similar two-stage volcanism in this region was also established for the neighboring large intraplate Afanasy Nikitin uplift based on the determination of the absolute age of the dredged basalts there [56]. Initially, the main plateau was formed about 80–73 Ma ago. Then, 6–13 Ma later, a 1200 m-high seamount of the same name was formed on the plateau as a result of magma outpouring from the chamber below the uplift, which drifted together with the lithospheric plate. All of the above is consistent with our assumption of two stages of formation of the studied seamount at the base of the western slope of the NER as a result of magmatic activity apparently associated with faults.

4. Conclusions

(1) The studied seamount appears to consist of two different-age fragments formed about 47 Ma and 23 Ma, respectively, 31 and 55 Ma after the main Ninetyeast Ridge massif. In the first stage, the main western part of the seamount was formed. Then, during the exploratory phase of magmatic activity, the volcanic structure expanded eastward;

(2) The explored seamount located at latitude 0.5° N and the volcano of the late Miocene age located to the south at latitude 10° S [16] are in the zone of one of the giant meridional faults that define the NER fault structure [8]. It is likely that the mechanism of formation of these two volcanic structures is somewhat the same, although the timing of formation differs significantly. As for the two volcanoes on the NER dome near 17° S [19], these appeared to be related to the underplating magmatism of the reactivation of this fault when the critical intraplate compression during continental collision was reached;

(3) The morphology of the studied seamount suggests that it was formed as a result of magma outpourings in the SW-NE strike-slip fault after the formation of the main NER massif in the zone of a giant meridional fault [24]. Presumably, these SW-NE strike-slip faults are second-order structures that apparently formed in the zone of the ancient meridional transform fault [12]. The process was complicated by the fact that shear deformations occurred along the fault during the relaxation of excess regional compression stress with a NW-SE vector in the body of the Indo-Australian lithospheric plate due to continental collision at its northern boundary. These shifts potentially created the local tensile fault zones necessary for this, along which the rise of magmatic material took place;

(4) The results of comprehensive studies performed in cruise #42 of the R/V *Akademik Boris Petrov* suggest rather long cyclic magmatic activity in the northern segment of the NER after 47 Ma already after the formation of its main massif at about 80 Ma.

In conclusion, we note, as well as other researchers [19,56], that the question of secondary magmatism, or its last stage in the Ninetyeast Ridge, remains open to discussion, as dredges of seamounts within it are needed to obtain a more definitive answer.

Author Contributions: Conceptualization, O.L.; methodology, O.L., A.I., I.V. and N.T.; software, A.I. and I.V.; validation, V.Y., O.L. and A.I.; formal analysis, V.Y. and O.L.; investigation, O.L., A.I., V.Y., I.V., Y.M., N.T. and V.Y.; resources, V.Y.; data curation, O.L. and V.Y.; writing—original draft preparation, O.L., A.I., N.T. and Y.M.; writing—review and editing, V.Y. and O.L.; visualization, Y.M., A.I., I.V. and, N.T.; supervision, V.Y. and O.L.; project administration, O.L. and V.Y.; funding acquisition, V.Y. All authors have read and agreed to the published version of the manuscript.

Funding: This work was performed within the framework of IO RAS No. FMWE-2021-0005 and GIN RAS No. FMMG-2023-0005. The APC was partially funded by Instituto Potosino de Investigación Científica y Tecnológica, A.C. and by grant CONACYT project A1-S-29604 to Vsevolod Yutsis.

Institutional Review Board Statement: Not applicable.

Informed Consent Statement: Not applicable.

Data Availability Statement: The original data are property of Shirshov Institute of Oceanology, it could be available to third parts after consideration of official request. The bathymetry data are available at the GEBCO_2019 Grid, https://www.gebco.net/data_and_products/gridded_bathymetry_data/ (accessed on 10 December 2022). Marine geomagnetic data are available at NCEI database https://www.ngdc.noaa.gov/mgg/trk/trackline (accessed on 15 December 2022).

Acknowledgments: This work was performed within the framework of IO RAS No. FMWE-2021-0005 and GIN RAS No. FMMG-2023-0005. The observations described have generally been made in cruise #42 of the R/V *Akademik Boris Petrov*. The authors are grateful for the support provided by colleagues who participated in the geophysical research, as well as the captain and crew of the vessel. The authors thank the anonymous reviewers for their valuable observations, which greatly improved the work. The authors are grateful to Graham Matthew Tippett for editing the English version of manuscript.

Conflicts of Interest: The authors declare no conflict of interest.

References

1. Koppers, A.A.P.; Watts, A.B. Intraplate seamounts as a window into deep earth processes. *Oceanography* **2010**, *23*, 42–57. [CrossRef]
2. Hedervari, P.A. Possible submarine volcano near the central part of Ninety-East Ridge, Indian Ocean. *J. Volcanol. Geotherm. Res.* **1982**, *13*, 199–211. [CrossRef]
3. Mukhopadhyay, R.; Batiza, R. Basinal Seamounts and Seamount Chains of the Central Indian Ocean: Probable Near-Axis Origin from a Fast-Spreading Ridge. *Mar. Geoph. Res.* **1994**, *16*, 303–314. [CrossRef]
4. Mukhopadhyay, R. Post-Cretaceous intraplate volcanism in the Central Indian Basin. *Mar. Geol.* **1998**, *151*, 135–142. [CrossRef]
5. Das, P.; Iyer, S.D.; Kodagali, V.N.; Krishna, K.S. Distribution and Origin of Seamounts in the Central Indian Ocean Basin. *Mar. Geod.* **2005**, *28*, 259–269. [CrossRef]
6. Iyer, S.D.; Das, P.; Kalangutkar, N.G. Seamounts—Windows of opportunities and the Indian scenario. *Curr. Sci.* **2012**, *102*, 1382–1391.
7. Homrighausen, S.; Hoernle, K.; Wartho, J.-A.; Hauff, F.; Werner, R. Do the 85° E Ridge and Conrad Rise form a hotspot track crossing the Indian Ocean? *Lithos* **2021**, *398–399*, 106234. [CrossRef]
8. Royer, J.-Y.; Peirce, J.W.; Weissel, J.K. Tectonic constraints on the hot-spot formation of Ninetyeast Ridge. *Proc. ODP Sci. Res.* **1991**, *121*, 763–776. [CrossRef]
9. Krishna, K.S.; Abraham, H.; Sager, W.W. Tectonics of the Ninetyeast Ridge derived from spreading records in adjacent ocean basins and age constraints of the ridge. *J. Geophys. Res.* **2012**, *117*, B04101. [CrossRef]
10. Nobre Silva, G.; Weis, D.; Scoates, J.S.; Barling, J. The Ninetyeast Ridge and its relation to the Kerguelen, Amsterdam and St. Paul Hotspots in the Indian ocean. *J. Petrol.* **2013**, *54*, 1177–1210. [CrossRef]
11. Frey, F.A.; Silva, I.G.N.; Huang, S.; Pringle, M.S.; Meleney, P.R.; Weis, D. Depleted components in the source of hotspot magmas: Evidence from the Ninetyeast Ridge (Kerguelen). *Earth Planet. Sci. Let.* **2015**, *426*, 293–304. [CrossRef]
12. Sushchevskaya, N.M.; Levchenko, O.V.; Dubinin, E.P.; Belyatsky, B.V. Ninetyeast Ridge: Magmatism and geodynamics. *Geochem. Int.* **2016**, *54*, 237–256. [CrossRef]
13. Levchenko, O.V.; Sushchevskaya, N.M.; Marinova, Y.G. The Nature and Evolution of the Ninetyeast Ridge: A Key Tectonic and Magmatic Feature of the East Indian Ocean. *Geotectonics* **2021**, *55*, 194–218. [CrossRef]
14. Von der Borch, C.C.; Christopher, C.; Sclater, J.G.; Veevers, J.J.; Hekinian, R.; Thompson, R.W.; Pimm, A.C.; McGowran, B.; Gartner, S., Jr.; Johnson, D.A. *Initial Reports of the Deep-Sea Drilling Project*; US Government Printing Office: Washington, DC, USA, 1974; Volume 22, p. 890.
15. Weissel, J.; Peirce, J.; Taylor, E.; Alt, J. *Proceedings of the ODP: Scientific Results*; Ocean Drilling Program: College Station, TX, USA, 1991; Volume 121, p. 990.
16. Kumar, R.T.; Windley, B.F. Spatial variations of effective elastic thickness over the Ninetyeast Ridge and implications for its structure and tectonic evolution. *Tectonophysics* **2013**, *608*, 847–856. [CrossRef]
17. Sreejith, K.M.; Krishna, K.S. Magma production rate along the Ninetyeast Ridge and its relationship to Indian Plate motion and Kerguelen Hot Spot activity. *Geophys. Rev. Lett.* **2015**, *42*, 1105–1112. [CrossRef]
18. Evsyukov, Y.D. Morphology of the Ninetyeast Ridge north of the equator. *Oceanology* **2003**, *43*, 270–275.
19. Kopf, A.; Klaeschen, D.; Weinrebe, W.; Flueh, E.R.; Grevemeyer, I. Geophysical evidence for late stage magmatism at the central Ninetyeast ridge, Eastern Indian Ocean. *Mar. Geophys. Res.* **2001**, *22*, 225–234. [CrossRef]

20. Sager, W.W.; Bull, J.M.; Krishna, K.S. Active faulting on the Ninetyeast Ridge and its relation to deformation of the Indo-Australian plate. *J. Geophys. Res.* **2013**, *118*, 13755–13782. [CrossRef]
21. Levchenko, O.V.; Sborshchikov, I.M.; Marinova, Y.G. Tectonics of the Ninetyeast Ridge. *Oceanology* **2014**, *54*, 231–244. [CrossRef]
22. Kashintsev, G.L.; Levchenko, O.V. Miocene volcanism of the Ninetyeast Ridge. *Dokl. Earth Sci.* **2009**, *428*, 1054–1057. [CrossRef]
23. Bezrukov, P.I.; Neprochnov, Y.P. (Eds.) *Geology and Geophysics of the Sea Floor in the Eastern Indian Ocean*; Nauka: Moskow, Russia, 1981; 255p. (In Russian)
24. Kashintsev, G.L. Aspects of magmatism of the Ninetyeast Ridge. *Oceanology* **2001**, *41*, 413–418.
25. Levchenko, O.V.; Shapovalov, S.M. Return of Russian Oceanographers to the Indian Ocean: Multidisciplinary Study during the 42nd Cruise of the Research Vessel Akademik Boris Petrov. *Oceanology* **2019**, *59*, 164–167. [CrossRef]
26. GEBCO (General Bahtymetric Chart of the Oceans). The GEBCO_2019 Grid. Available online: https://www.gebco.net/data_and_products/gridded_bathymetry_data/ (accessed on 10 December 2022).
27. Multibeam Report for RR1510. Ship Name: Roger Revelle: Chief Scientist: None: Source Organization: UNOLS R2R: Start Date: 8 July 2015: End Date: 2 August 2015. Available online: https://www.ngdc.noaa.gov/ships/roger_revelle/RR1510_mb.html (accessed on 15 December 2022).
28. Stein, S.; Okal, E.O. Seismicity and tectonics of the Ninetyeast Ridge area: Evidence for internal deformation of the Indian plate. *J. Geophys. Res.* **1978**, *83*, 2233–2246. [CrossRef]
29. Petroy, D.E.; Wiens, D.A. Historical seicmicity and implications for diffuse plate convergence in the northeast Indian Ocean. *J. Geophys. Res.* **1989**, *94*, 12301–12319. [CrossRef]
30. Bastia, R.; Radhakrishna, M.; Das, S.; Kale, A.S.; Catuneanu, O. Delineation of the 85° E ridge and its structure in the Mahanadi Offshore Basin, Eastern Continental Margin of India (ECMI), from seismic reflection imaging. *Mar. Pet. Geol.* **2010**, *27*, 1841–1848. [CrossRef]
31. Satriano, C.; Kiraly, E.; Pascal Bernard, P.; Vilotte, J.-P. The 2012 Mw 8.6 Sumatra earthquake: Evidence of westward sequential seismic ruptures associated to the reactivation of a N-S ocean fabric. *Geophys. Res. Lett.* **2012**, *39*, L15302. [CrossRef]
32. Caress, D.W.; Chayes, D.N. MB-System Version 5.5.2252. Open Source Software Distributed from the MBARI and L-DEO Web Sites, 2000–2015. 2015. Available online: https://www.mbari.org/products/research-software/mb-system/ (accessed on 20 November 2022).
33. GEODAS. Available online: https://www.ncei.noaa.gov/maps/bathymetry/ (accessed on 20 November 2022).
34. Conrad, O.; Bechtel, B.; Bock, M.; Dietrich, H.; Fischer, E.; Gerlitz, L.; Wehberg, J.; Wichmann, V.; Böhner, J. System for Automated Geoscientific Analyses (SAGA) v. 2.1.4. *Geosci. Model Dev.* **2015**, *8*, 1991–2007. [CrossRef]
35. Catuneanu, O. *Principles of Sequence Stratigraphy*, 2nd ed.; Elsevier: Amsterdam, The Netherlands, 2022; 375p.
36. Mitchum, R.M. Seismic stratigraphy and global changes of sea level, Part 11: Glossary of terms used in seismic stratigraphy. In *Seismic Stratigraphy—Applications to Hydrocarbon Exploration*; Payton, C.E., Ed.; AAPG Memoir 26: Tulsa, OK, USA, 1977; pp. 205–212.
37. Vail, P.R.; Mitchum, R.M.; Todd, R.G.; Widmier, J.M.; Thompsom, S.; Sangree, J.B.; Bubb, J.N.; Hailelid, W.G. Seismic stratigraphy and global changes in sea level. In *Seismic Stratigraphy—Applications to Hydrocarbon Exploration*; Payton, C.E., Ed.; AAPG Memoir 26: Tulsa, OK, USA, 1977; pp. 49–212.
38. Clemens, S.C.; Kuhnt, W.; LeVay, L.J.; Anand, P.; Ando, T.; Bartol, M.; Bolton, C.T.; Ding, X.; Gariboldi, K.; Giosan, L.; et al. Indian Monsoon Rainfall. In Proceedings of the International Ocean Discovery Program, College Station, TX, USA, 29 November 2014–29 January 2015; International Ocean Discovery Program: College Station, TX, USA, 2016; Volume 353. [CrossRef]
39. Lewis, K.W. Slumping on a continental slope inclined at 1°–4°. *Sedimentology* **1971**, *16*, 97–110. [CrossRef]
40. National Centers for Environmental Information, NCEI Database. NGDC. Available online: https://www.ngdc.noaa.gov/mgg/trk/trackline (accessed on 15 December 2022).
41. Okubo, Y.; Matsunaga, T. Curie point depth in northeast Japan and its correlation with regional thermal structure and seismicity. *J. Geophys. Res. Solid Earth* **1994**, *99*, 22363–22371. [CrossRef]
42. Thébault, E. Magnetic Anomalies, Interpretation. In *Encyclopedia of Solid Earth Geophysics. Encyclopedia of Earth Sciences Series*; Gupta, H.K., Ed.; Springer: Dordrecht, The Netherlands, 2011. [CrossRef]
43. Vine, F.J.; Matthew, D.H. Magnetic anomalies over oceanic ridges. *Nature* **1963**, *199*, 947–949. [CrossRef]
44. Hulot, G.; Olsen, N.; Sabaka, T.J. The Present Field, Chap. 6, Vol. 5. In *Geomagnetism*; Kono, M., Ed.; Treatise on Geophysics; Elsevier: Amsterdam, The Netherlands, 2007; pp. 33–72.
45. Baranov, V. *Potential Fields and Their Transformations in Applied Geophysics*; Borntraeger: Berlin, Germany, 1975; ISBN 3443130089.
46. Helbig, K. Some integrals of magnetic anomalies and their relationship to the parameters of disturbing body. *Z. Geophys.* **1962**, *29*, 83–97.
47. Caratori Tontini, F.; Pedersen, L.B. Interpreting magnetic data by integral moments. *Geophys. J. Int.* **2008**, *174*, 815–824. [CrossRef]
48. Valyashko, G.M.; Ivanenko, A.N.; Czerniawski, G.E.; Lukyanov, S.V. Interpretation Procedure of Marine Magnetic Data: Topical Problems. In *Anomalous Magnetic Field of the World Ocean*; Gorodnitsky, A.M., Ed.; CRC Press: Boca Raton, FL, USA, 1995; pp. 21–66.
49. Spector, A.; Grant, F.S. Statistical models for interpreting aeromagnetic data. *Geophysics* **1970**, *35*, 293–302. [CrossRef]
50. Kelemework, Y.; Fedi, M.; Milano, M. A review of spectral analysis of magnetic data for depth estimation. *Geophysics* **2021**, *86*, J33–J58. [CrossRef]

51. Van Hinsbergen, D.J.J.; de Groot, L.V.; van Schaik, S.J.; Spakman, W.; Bijl, P.K.; Sluijs, A.; Langereis, C.G.; Brinkhuis, H. A Paleolatitude Calculator for Paleoclimate Studies (model version 2.1). *PLoS ONE* **2015**, *10*, e0126946. [CrossRef]
52. Levchenko, O.V.; Milanovsky, V.E.; Popov, A.A. Sediment thickness map and tectonics of the Distal Bengal Fan. *Oceanology* **1993**, *33*, 269–275.
53. Ogg, J. Geomagnetic Polarity Time Scale. In *Geologic Time Scale*, 1st ed.; Elsevier: Amsterdam, The Netherlands, 2022; pp. 159–192. [CrossRef]
54. Coffin, M.F. Emplacement and subsidence of Indian Ocean Plateaus and submarine ridges. In *Synthesis of Results from Scientific Drilling in the Indian Ocean*; Monograph 70; American Geophysical Union: Washington, DC, USA, 1992; pp. 115–125.
55. Ninkovich, D. Distribution, age and chemical composition of tephra layers in deep-sea sediments of western Indonesia. *J. Volcanol. Geotherm. Res.* **1979**, *5*, 67–86. [CrossRef]
56. Krishna, K.S.; Bull, J.M.; Ishizuka, O.; Scrutton, R.A.; Jaishankar, S.; Banakar, V.K. Growth of the Afanasy Nikitin seamount and its relationship with the 85° E Ridge, northeastern Indian Ocean. *J. Earth Syst. Sci.* **2014**, *123*, 33–47. [CrossRef]